Journal of Power Sources 667 (2026) 239216

Contents lists available at ScienceDirect

Journal of Power Sources

journal homepage: www.elsevier.com/locate/jpowsour

Heterogeneous graphite felt electrodes decorated with nanostructured graphitic carbon nitride for enhanced redox kinetics in vanadium redox flow batteries

Iqra Shaheen [a,1], Wei-Hao Chiu [b,1], Yu-Xian Lee [a,1], Shih-Hsuan Chen [a], Jen-Fu Hsu [d], Kun-Mu Lee [a,b,c,d,*]

[a] Department of Chemical and Materials Engineering, Chang Gung University, Taoyuan, 33302, Taiwan
[b] Center for Sustainability and Energy Technologies, Chang Gung University, Taoyuan, 33302, Taiwan
[c] College of Environment and Resources, Ming Chi University of Technology, New Taipei City, 24301, Taiwan
[d] Division of Neonatology, Department of Pediatrics, Chang Gung Memorial Hospital, Linkou, Taoyuan, 33305, Taiwan

HIGHLIGHTS

- Urea thermal polymerization enables tunable decoration of g-C_3N_4 nanostructures on GF.
- Layered g-C_3N_4 structures increase surface area and enhance electrode wettability.
- Synergistic structure and chemistry improve durability and energy efficiency.
- g-C_3N_4/GF electrodes exhibit high stability and long-term VRFB reliability.

GRAPHICAL ABSTRACT

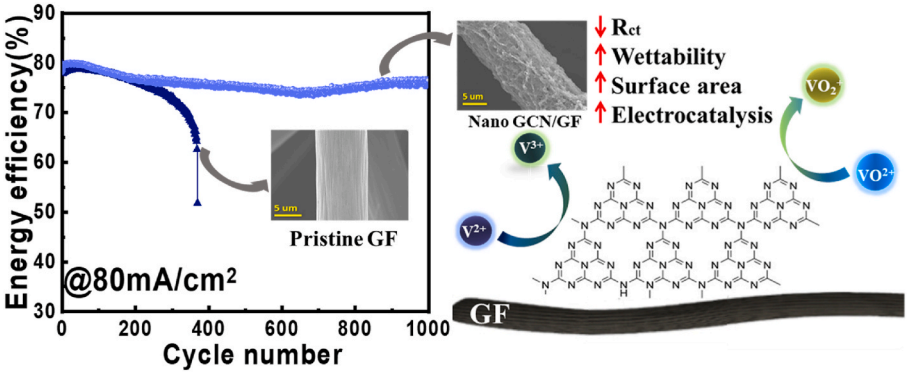

ARTICLE INFO

Keywords:
Graphite felt
g-C_3N_4
Thermal polymerization
Charge-transfer resistance
Surface modification
Hydrophilicity
Electrochemical activity

ABSTRACT

Graphite felt (GF) is a porous carbonized polymer used as multifunctional electrodes in energy and environmental electrochemical devices. Despite its high surface area, limited surface-active sites reduce catalytic activity. Furthermore, its intrinsic hydrophobicity requires hydrophilic pretreatment for effective electrochemical performance. Graphitic Carbon Nitride (g-C_3N_4) enables structural regulation by creating conjugated systems through its electronic structure, thereby expanding its multifunctionality and applications in electrode materials. An optimal g-C_3N_4 concentration on the GF ensures better conductivity, resulting in higher electrochemical activity. This study used thermal polymerization to decorate GF with g-C_3N_4 (GCN/GF), and nano GCN/GF electrode showed excellent hydrophilicity, lowest charge-transfer resistance (R_{ct}), and high electrochemical activity. An optimally decorated g-C_3N_4 showed minimal agglomeration, better distribution on GF surfaces, and superior active sites for VO^{2+}/VO_2^+ redox reaction. Its uniform decoration of g-C_3N_4 facilitated charge transport,

* Corresponding author. Department of Chemical and Materials Engineering, Chang Gung University, Taoyuan, 33302, Taiwan.
E-mail address: kmlee@mail.cgu.edu.tw (K.-M. Lee).
[1] They contributed equally to this work.

https://doi.org/10.1016/j.jpowsour.2025.239216
Received 1 September 2025; Received in revised form 15 December 2025; Accepted 26 December 2025
Available online 2 January 2026
0378-7753/© 2025 Published by Elsevier B.V.

enhanced hydrophilicity, and improved electrolyte access, reducing electrochemical polarization during active species transfer, and energy efficiency improved to 84.13 % at 80 mA cm^{-2}. The long-term cycling performance confirmed the durability of the vanadium redox flow battery (VRFB) with the nano GCN/GF electrode, exhibiting negligible degradation for 1000 cycles. These findings highlight the potential of g-C_3N_4 as a cost-effective alternative to noble metals for high-performance VRFB electrodes.

1. Introduction

The rapid development of industrialization and extensive use of fossil fuels produce numerous greenhouse gases, accelerating the greenhouse effect on Earth, causing global warming, and leading to extreme climate change worldwide [1]. The United Nations Intergovernmental Panel on Climate Change (IPCC) reported that the global average temperature will rise in the next 20 years. Many countries are transforming their energy systems to reduce carbon emissions as a shared goal, aiming for net-zero carbon emissions by 2050. Governments are seeking alternative energy sources, emphasizing renewable energy to minimize reliance on petroleum and reduce greenhouse gas emissions [2]. While renewable energy has low pollution, climate conditions, and time zones impact power generation efficiency, leading to unstable energy output. Large-scale energy storage facilities are essential. Physical storage provides large-scale capability, high energy conversion efficiency, and longevity; yet, geographical limitations and higher initial costs hinder its popularity and development [3]. The global trend towards enhanced chemical energy storage has significantly increased the development of various secondary battery types [4]. Flow batteries store energy chemically, and their independently scalable power (electrical output) and energy (storage capacity) provide design flexibility, high safety, long discharge times, fast response, and long cycle life, with ongoing advancements across various flow-battery types [5]. Vanadium redox flow batteries (VRFBs) have an expandable energy storage capacity and relatively good safety compared to other energy storage devices, making them more efficient [6]. VRFBs consist of two carbon-based electrodes, a separator, two pumps, and two electrolyte tanks [7]. Electrode selection depends on factors like oxidation stability, design flexibility, cost-effectiveness, and high electrical conductivity.

In recent years, the development of VRFBs has attracted much attention. Many research groups have investigated various elements to enhance battery efficiency, including optimizing flow channels, utilizing electrolyte additives, modifying exchange membranes, and improving electrode surfaces. Carbon felt (CF) and graphite felt (GF) are both widely used as electrode substrates in VRFBs due to their high conductivity and porous structure. Due to its superior conductivity attributed to the graphitized carbon structure, graphite felt (GF) is the most favorable to date. However, the poor electrochemical activity and reversibility of graphite felt limit the overall performance of the VRFB cell [8]. Recent studies on CF-based electrodes have demonstrated that surface activation, heteroatom doping, and nanomaterial coatings can significantly enhance redox kinetics and wettability [9–13]. Building on these insights, the present work focuses on GF modification, aiming to achieve similar catalytic enhancement while maintaining the structural robustness of GF. Multiple strategies have been introduced to modify GF electrodes, including surface treatments (thermal, plasma, chemical), carbon depositions (CNT, C nanoparticles), or metal depositions (Au, Pt, Bi, Cu) [14–16], perovskite modifiers such as $AZrO_3$ (A = Ca, Sr, Ba) and $SrBO_3$ (B = Ti, Zr, Hf) [17,18]. Low-cost metal oxide catalysts such as SnO_2, WO_3, TiO_2, CeO_2, and PbO_2, known for their strong corrosion resistance, abundant active sites, and high hydrophilicity, are frequently utilized for modifying electrodes [19–22]. However, they face challenges like agglomeration, poor bonding, and nano-crystallization issues, which significantly limit their catalytic performance.

Various groups have attempted different electrode modification methods to improve their properties, and the energy efficiencies achieved at different current densities of graphite felts after modification with C/N based materials and metal oxides are shown in Fig. 1. Kabtamu, D.M. et al. [23] introduced Nickel tungstate ($NiWO_4$) nanowires to modify graphite felt (GF). The $NiWO_4$-modified heat-treated graphite felt ($NiWO_4$-HGF) showed superior catalytic activity and redox performance reversibility. Bao, J. et al., [24] proposed a novel hierarchical carbon shell-supported carbon nitride, grown in situ on pristine graphite felt (HCS/C_3N_4@GF), and significantly enhanced physicochemical properties and electrochemical performance. Li, Q. et al., [25] decorated GF with $Ti_3C_2T_X$/Bi using a simple dropping method and improved the electrochemical performance of the electrode. Ji, J. et al., [26] modified graphite felt (GF) by incorporating a mesoporous N-doped carbon structure. This architecture facilitates the mass transfer of vanadium ions and improves electrochemical performance even at higher current densities, thus enhancing the reactivity and reversibility of redox kinetics. Zhang, Z. et al., [27] used KOH as an etchant to etch the surface of GF with varying mass ratios. Wei, L. et al., [16] used different concentrations of copper sulfate ($CuSO_4$) added to the various electrolytes to form Cu nanoparticles on the surface of the GF during the electrolysis process. Yun, N. et al., [28] used nickel nitrate hexahydrate ($Ni(NO_3)_2{\cdot}6H_2O$) as a precursor to attach on the surface of the GF, followed by the use of Argon sintering at different temperatures. However, the main issues with electrodes include material agglomeration, safety risks, and phase variations during charge–discharge cycles, as a result of bad chemical stability [29,30].

Graphitic carbon nitride (g-C_3N_4), a Well-known 2-D semiconductor for its exceptional chemical and physical stability, environmental friendliness, and pollution-free benefits, is driving significant research in energy storage [31]. It offers a simple preparation process and easy material optimization, consisting of triazine (C_3N_3) or s-triazine (C_6N_7) rings interconnected by nitrogen bridges, creating a 2-D network with vacancies where carbon and nitrogen atoms are absent. There are four primary synthesis methods for g-C_3N_4: thermal polymerization, solvothermal, template-assisted, and photopolymerization. Among these, it can be easily fabricated through the thermal polymerization of nitrogen-rich precursors such as melamine, dicyandiamide, cyanamide, urea, thiourea, and ammonium thiocyanate [32–34]. It has abundant amino and Lewis basic groups with high nitrogen density, facilitating efficient charge transfer and electrolyte penetration. Moreover, its graphite-like layered structure and large π bonds enhance versatility in creating multifunctional materials with various dimensions, doping, and conjugated systems [35]. These traits expand its potential in energy storage devices. It has a moderate band gap of 2.7–2.8 eV, enabling visible light absorption around 450–460 nm [36], and it is thermally stable up to 600 °C in air, which is attributed to aromatic C–N heterocycles. g-C_3N_4 is a metal-free, earth-abundant, nontoxic material used in pollutant degradation, water splitting, and solar energy transfer due to its strong photocatalytic and opto-electronic properties [37–40]. Daugherty, M.C. et al., [41] Synthesized nitrogen-doped graphene quantum dots (GQDs) and g-C_3N_4 quantum dots using the solid-phase microwave-assisted (SPMA) method with varying citric acid to urea ratios. They struggled with complex and scalable synthesis, long-term acidic conditions stability, and high current density efficiency. Issues such as GQD aggregation, high dopant costs, and energy-intensive processes hinder commercial viability. Future initiatives must enhance synthesis techniques, retention capacity rates, electrode durability, catalyst dispersion, and cost-effectiveness. However, g-C_3N_4 can encapsulate and safeguard other materials. By serving as protective shields, they shield sensitive surfaces from external influences, such as harsh environments

and chemical reactions, thereby maintaining the integrity and performance of the encapsulated materials. This study aims to enhance the electrochemical properties, hydrophilicity, and specific surface area of graphite felts by decorating them with g-C_3N_4 through a simple thermal polymerization process, thereby promoting the growth of layered g-C_3N_4 structures on the surface. As it has inherent chemical stability and a porous structure, it increases the specific surface area and generates more nitrogen-containing groups to improve the hydrophilicity of GF. The electrochemical performance of the reported graphite felts after modification using carbon/nitrogen-based materials and metal oxides, compared with this work, is summarized in Table S1.

2. Experimental

2.1. Preparation of the electrode

In this section, the preparations of pristine graphite felt (GF) and g-C_3N_4 decorated graphite felt (GCN/GF) were described in detail and shown in Fig. 2.

2.1.1. Preparation of pristine graphite felt (GF)

First, cut the graphite felt (ShenEnergy Tech Ltd.) into pieces measuring 0.5 cm^3 (1 cm × 1 cm x 5 mm). Then, to eliminate impurities and organic contaminants from the graphite felt's surface, it was immersed in ethanol and subjected to ultrasonic washing for 10 min. After cleaning, the graphite felt was dried in an oven (DENG YNG (DO V30)) at 80 °C for 12h. To enhance the hydrophilicity of the GF surface, ozone treatment was performed using a UV-ozone machine (Jelight (42A)) for 20 min.

2.1.2. Preparation of g-C_3N_4 decorated graphite felt (GCN/GF)

The preparation of g-C_3N_4 decorated graphite felt (GCN/GF) includes steps of pre-adsorption followed by thermal polymerization. To ensure surface cleanliness and hydrophilicity prior to g-C_3N_4 deposition, the graphite felt underwent the same pretreatment as the pristine GF, including ethanol washing and ozone treatment. This process introduced oxygenated functional groups onto the GF surface, enhancing the interaction with urea precursors and facilitating uniform deposition and strong adhesion during subsequent thermal polymerization. Different weights of urea particles (0.25 g, 0.50 g, and 0.75 g, J.T. Baker/99.0 %) were added to 20 ml of ethanol solution (ECHO Chemical Co., Ltd./99.5 %) and ultrasonically dispersed, considering the limited solubility of urea in ethanol (5 g urea per 100 ml ethanol) for pre-adsorption. Subsequently, the pristine GF was immersed in the urea-ethanol solution and placed in the muffle furnace (DENG YNG (DF40)) at 90 °C to evaporate the ethanol. When the ethanol had evaporated, the urea precipitated onto the GF, denoted as Urea/GF (U-GF). To ensure uniform sintering and minimize particle movement during thermal polymerization, the U-GF was placed in the crucible with additional urea (1.25 g, 2.50 g, and 4.00 g) and zirconium balls as spacers. After the aluminium-foil-sealed crucible was placed in the muffle furnace, the thermal polymerization reaction occurred at a sintering temperature of 550 °C for 4 h with a 2 °C/min heating rate. After the reaction, the cool-down samples were washed with deionized water to remove the excess reactants, after which the graphite felts were dried in an oven at 80 °C for 12h. Finally, graphite-phase carbon nitride decorated GFs (GCN/GFs) at concentrations of 0.2M, 0.4M, and 0.6M were obtained using urea amounts of 0.25 g, 0.50 g, and 0.75 g, respectively. The preparation process flow of the in-situ growth of g-C_3N_4 decorated graphite felt is illustrated in Fig. 2a. For completeness, it is worth noting that physically mixed g-C_3N_4 powder was not adopted as a control sample. Prior studies have shown that physically deposited g-C_3N_4 exhibits weak adhesion and non-uniform coverage on carbon-based electrodes, leading to rapid detachment under electrolyte flow. In contrast, the in situ thermal polymerization method used here forms a chemically bonded, conformal decoration that ensures uniform dispersion and long-term operational stability, which is essential for VRFB electrodes.

2.2. Material characterization

Scanning electron microscopy (SEM, Hitachi SU8010) and energy-dispersive spectroscopy (EDS) were employed to investigate the morphology and elemental composition of the samples. The crystal structure was analyzed using an X-ray diffractometer (XRD, Rigaku). Fourier-transform infrared (FTIR) spectra were collected by a Bruker Model spectrometer (Tensor 27) in the range of 700~3600 cm^{-1}. The surface area and pore diameter were analyzed using the Brunauer-Emmett-Teller (BET) measurement (SHIMADZU, AUX220). The hydrophilicity of the samples was investigated using a contact angle goniometer (Sindatek Instrument Co., Ltd., 100SB).

2.3. Electrochemical measurement

The electrochemical tests, including cyclic voltammetry (CV) and electrochemical impedance spectroscopy (EIS), were conducted using an Autolab modular system (PGSTAT302N, Metrohm Co., Ltd.) using a

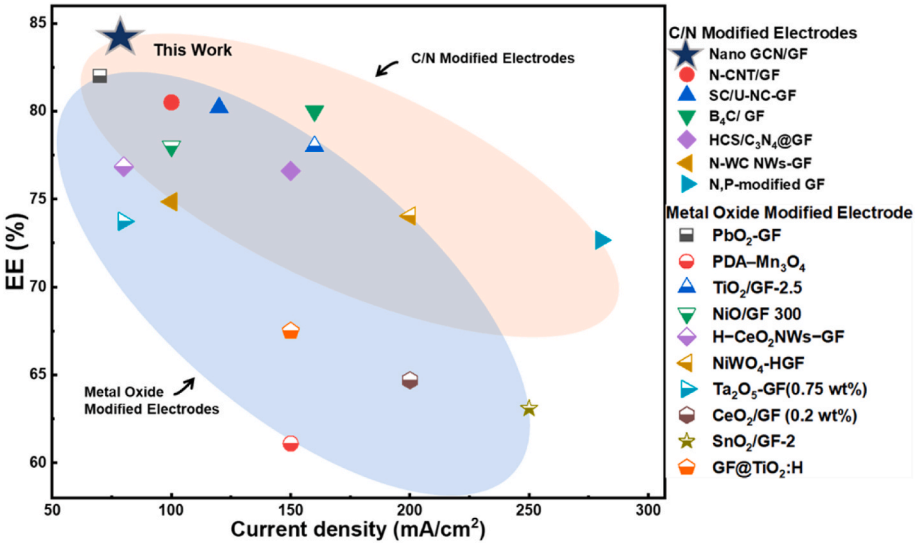

Fig. 1. EE of the modified graphite felt (GF) electrode in VRFBs from the literature.

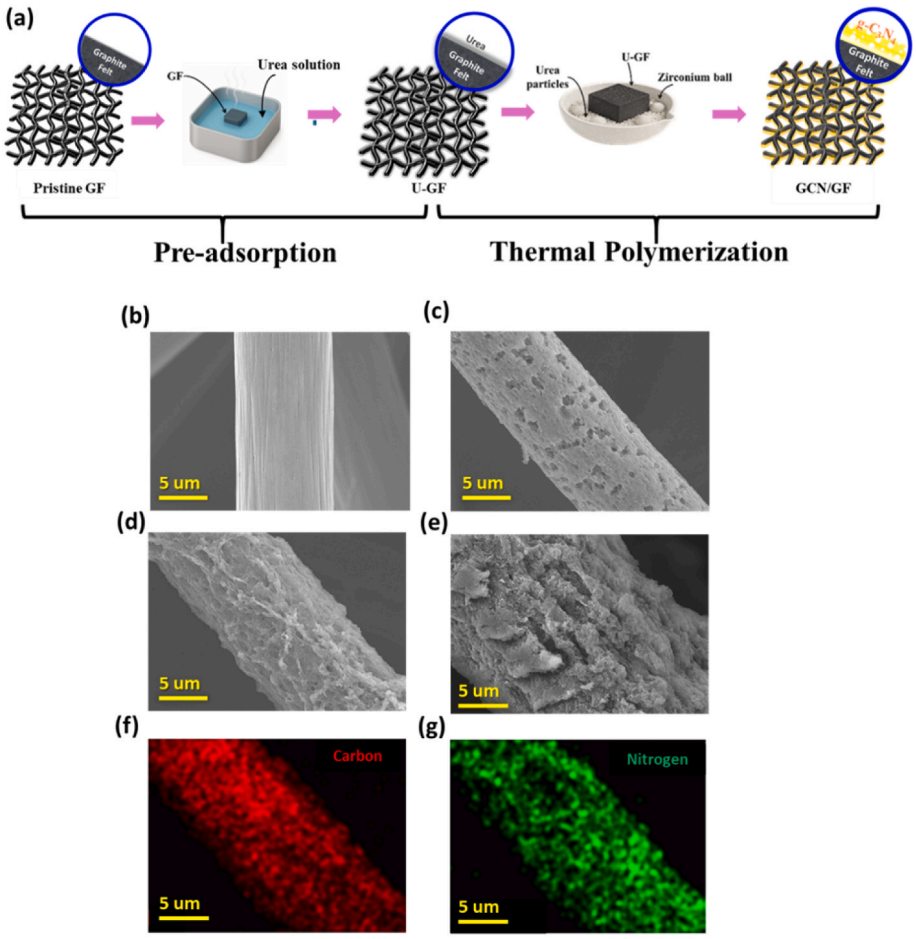

Fig. 2. (a) Illustration of the in-situ growth process of graphite-phase carbon nitride decorated graphite felt (GCN/GF). SEM images of (b) pristine graphite felt (GF), (c) porous GCN/GF, (d) nano GCN/GF, and (e) macro GCN/GF. (f) Carbon and (g) nitrogen EDS elemental mappings of nano GCN/GF.

standard three-electrode configuration, in which the prepared GF (working area = 0.785 cm^2), platinum (MAT-G6, Matsusada precision), and Ag/AgCl (RE-05, Matsusada precision) acted as the working electrode, counter electrode and the reference electrode, respectively. For CV measurement, the electrolyte consisted of a mixture of 0.05 M vanadium sulfate ($VOSO_4$, UBIQ Technology Co., Ltd./99.0 %) and 2 M sulfuric acid (H_2SO_4, Honeywell Fluka/98 %). The CV scanning potential ranged from 0 to 1.6 V with a scanning rate of 5 mV/s, and the current magnitude of the redox peaks, along with the potential difference of the redox reaction (ΔE) of each sample, were compared to determine the electrochemical properties. The EIS measurement was conducted at a potential of 0.8 V, with a frequency range of 10^{-2} Hz–10^5 Hz and an amplitude of 10 mV.

2.4. Charge–discharge test

A charge-discharge test was conducted using a flow cell on a battery test system NEWARE (CT-4008T) with a voltage range of 0.7–1.6V. The composition of the single cell used in this experiment is shown in Figure S1 g-C_3N_4 decorated graphite felt (5 cm × 5 cm) was used as positive and negative electrodes; for comparison, with decorated GFs, pristine graphite felt was also assembled as a positive or negative electrode in the same cell system. Positive and negative electrodes were placed in a polytetrafluoroethylene framework, which was separated by the ion-exchange membrane (model 102, ShenEnergy Tech Ltd.). Copper sheets and graphite plates were used as current collectors. Cell components were fastened between two endplates with fastening bolts. A mixed solution of 1.6M vanadyl sulfate and 3M sulfuric acid (H_2SO_4) was used as the original electrolyte. A volume of 50 mL was used for each of the two independent storage tanks, and the electrolyte was pumped into a cell at a flow rate of 0.1 L/min. The working area of the single cell was 5 cm × 5 cm. Different current density tests were performed at low to high current densities of 40 mA/cm^2, 60 mA/cm^2, 80 mA/cm^2, 100 mA/cm^2, 120 mA/cm^2, and 140 mA/cm^2. Three cycles were performed at each current density, and the coulombic efficiency (CE), voltage efficiency (VE), and energy efficiency (EE) were used to analyze the charge and discharge performance calculated by the following equations:

Coulombic efficiency (CE):

$$CE = \frac{Q(discharg)}{Q(charg)} \times 100\%$$

Voltage efficiency (VE):

$$VE = \frac{Vcc(discharg)}{Vcc(charg)} \times 100\%$$

Energy efficiency (EE):

$$EE = \eta C \times \eta V \times 100\%$$

3. Results and discussion

3.1. Material characterization analysis

In this section, the material characterization and performance evaluation of pristine graphite felt (GF) and g-C_3N_4 decorated graphite felt

(GCN/GF) are described in detail.

3.1.1. Microstructural surface analysis

The morphologies of pristine GF and a series of decorated GCN/GF samples with urea concentration [y M (y = 0.2, 0.4, 0.6)] were investigated by SEM and EDS, as shown in Fig. 2. The pristine graphite felt is a flat, cylindrical, smooth surface fiber, as shown in Fig. 2b. However, the incorporation of g-C_3N_4 structures, which contain nitrogen-rich groups (such as amino and imine), enhances the surface functionality of GF and increases the surface area and porosity, providing more reaction sites. At high temperatures, the urea on the surface of the graphite felt sintered, producing ammonia and carbon dioxide. The gas overflow led to surface structure damage and formed a surface structure on GF, which was observed in SEM images of decorated GFs. In Fig. 2c, the formation of surface etchings and holes during gas spillage is shown, indicating that a 0.2 M concentration was not entirely covered on GF due to an insufficient urea precursor, which was unable to decorate it properly, resulting in a porous GCN/GF. As the ratio was increased to 0.4M, the surface seemed decorated with the flake structure of g-C_3N_4, which was evenly grown as nanostructures on the GF surface, as seen in the SEM images of Fig. 2d and categorized as nano GCN/GF. As the ratio was further increased to 0.6 M, it over-aggregated due to the excessive urea precursor and formed lumps during the growth process, which seemed like macrostructures, and the GF fibers became thicker due to the over-decoration of g-C_3N_4 (Fig. 2e), given as macro GCN/GF. It was easy to peel off in large quantities during the cleaning process, and the over-aggregation of g-C_3N_4 reduced the surface area of reactivity, affecting electron transfer. Furthermore, to provide quantitative confirmation of g-C_3N_4 loading, thermogravimetric analysis (TGA) was conducted (Fig. S2). Since pristine GF shows negligible mass loss below 800 °C, whereas g-C_3N_4 fully decomposes between 550 and 650 °C, the additional weight loss observed in the composites directly reflects the deposited g-C_3N_4 content. The calculated loadings are ~3 wt% for porous GCN/GF (0.2 M), ~9 wt% for nano GCN/GF (0.4 M), and ~18 wt % for macro GCN/GF (0.6 M). The EDS spectrum of nano GCN/GF, on which the elements C and N are uniformly distributed, is also shown in Fig. 2(f & g). The red and green parts represent carbon and nitrogen elements, respectively, indicating the successful decoration of g-C_3N_4 on the GF's surface, which is consistent with the SEM results.

3.1.2. Microstructural analysis through XRD

To further study the morphology and structural characteristics of pristine GF and different structures of graphite-phase carbon nitride (g-C_3N_4) decorated GF (GCN/GF), samples were measured using XRD (X-ray Diffraction) crystallography analysis, as shown in Fig. 3a. Pristine GF exhibited two distinct broad diffraction peaks at 26.3° and 43.4°, which correlate with the planes (002) and (100), corresponding to the characteristic diffraction peaks of carbon in it, confirming that it has an amorphous carbon structure [42,43]. While g-C_3N_4 powder showed two distinct diffraction peaks at 13.1° and 27.6°, correlating with the plane (100) and (002), respectively, indexed in (JCPDS 87–1526) [44]. Different structures were formed from g-C_3N_4 through high-temperature synthesis using urea solutions with varying concentrations, as observed in SEM, and the successful incorporation of g-C_3N_4 onto GF is also confirmed by the presence of g-C_3N_4 peaks in the XRD results. As shown in the XRD analysis spectrum (Fig. 3a), significant (002) planar wrap-around peaks are observed at 26.3° for GF and 27.6°, corresponding to g-C_3N_4, which are also evident in all GCN/GF structure spectra with an increase in the proportion of precursor. For a more detailed analysis, this complex peak is deconvoluted for all GCN/GF structures, revealing that as the structure shifts from porous to macro GCN/GF, the intensity of the g-C_3N_4 peaks increases in both spectra, indicating a larger grain size with an increase in urea concentration on the GF surface. Variations in peak area or relative intensity are evident in this trend, highlighting the importance of an optimal proportion of urea in the precursor for grain size growth on the GF surface. Additionally, the peak at 13.1° corresponds to the (100) plane of g-C_3N_4 seen in these spectra. This peak is associated with the lamellar structure of the 3-5-triazine ring. In contrast, the plane of (002) is highly correlated with the degree of stacking of the covalent aromatic ring system. It can be predicted that as the proportion of the urea precursor increases, the degree of stacked lamellae of g-C_3N_4 also increases, along with the amount of adhesion to the surface of the GF.

3.1.3. Surface chemistry analysis through FTIR spectroscopy

Chemical bonds and functional groups in pristine graphite felt (GF) and various structures of graphite-phase carbon nitride decorated GF (GCN/GF) are also analyzed using FTIR spectroscopy, as shown in Fig. 3b. The spectra exhibited a prominent peak at 810 cm^{-1},

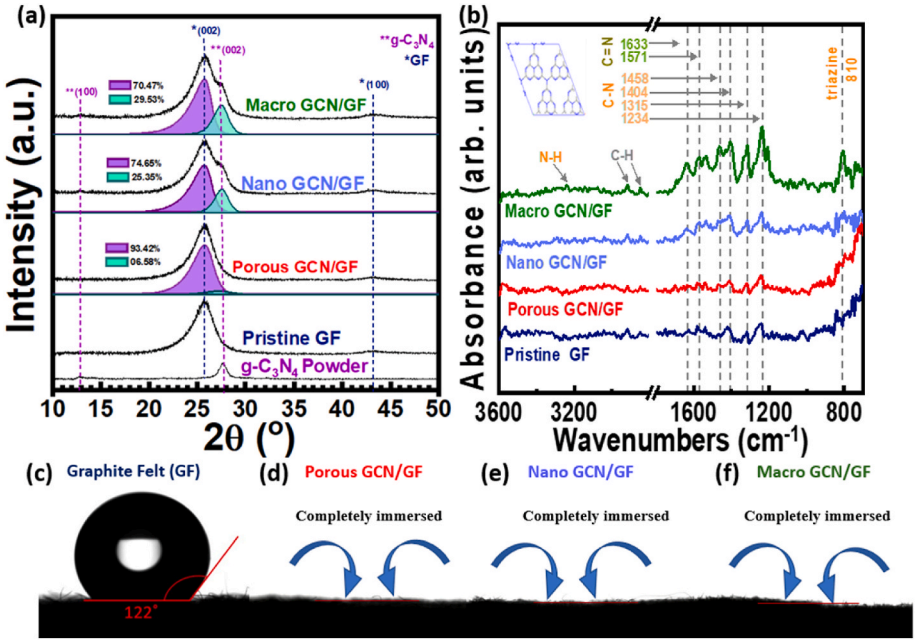

Fig. 3. (a) XRD patterns, (b) FTIR spectra, and (c–f) water contact angle of pristine graphite felt (GF) and various structures of graphite-phase carbon nitride decorated GF (GCN/GF).

corresponding to the breathing mode of the triazine rings. Additionally, a broad peak at 3200–3400 cm^{-1} is typical of the stretching vibrations of –NH groups [45]. Several absorption peaks in the 1200–1640 cm^{-1} region (1234, 1315, 1404, 1404,1458, 1571, and 1633 cm^{-1}) can be linked to C-N and C=N stretching vibrations of the CN aromatic repeating unit, further confirming the presence of g-C_3N_4 on the GF surface [46,47]. As observed in Fig. 3b, the intensity of peaks associated with g-C_3N_4 increases in decorated GF (GCN/GF) as the structure changes from porous GCN/GF to macro GCN/GF, consistent with XRD results and supporting the formation of GCN/GF structures on the GF.

3.1.4. Hydrophilicity test

The wettability of pristine GF and various structures of graphite-phase carbon nitride decorated GF (GCN/GF) was evaluated using the contact angle test. The wetting properties are determined by the contact angle of a water droplet on the surface of a sample, and the test is quick and non-destructive to the surface. Samples with good wettability have smaller contact angles. As shown in Fig. 3c, when a water droplet forms a nearly spherical surface on the GF surface with a contact angle of 122°, it indicates poor hydrophilicity, which hinders the penetration of the water droplet into the porous structure of pristine GF due to low polarity and smooth carbon surface, making it resistant to infiltration. In contrast, the GCN/GF exhibits a contact angle of 0° for the water droplets, indicating its excellent hydrophilicity. GCN/GFs contain nitrogen-rich structures with lone pairs that can facilitate adsorption due to the polar groups present in their structure. In Fig. 3d, porous GCN/GF show excellent hydrophilicity, as the water droplets flow into the porous structure directly, indicating that even a low concentration of g-C_3N_4 can effectively improve the hydrophilicity of the GF surface. Fig. 3e and f shows the contact angles of nano GCN/GF and macro GCN/GF, respectively; both achieve complete wetting. This is due to the increased roughness of decorated ultrafine structures, which enhances surface energy and improves interactions with the polar electrolyte. Consequently, the interfacial energy barrier decreases, promoting better wetting. Hence, g-C_3N_4 significantly enhances the hydrophilicity of GF, ensuring complete contact between the electrolyte and the electrode [48].

3.1.5. Surface chemistry analysis through XPS

XPS was employed as the primary quantitative tool to verify the decoration of g-C_3N_4 on graphite felt and to analyze the surface chemical states of the modified electrodes. The SEM and XRD observations demonstrate that the nano-sized flake-like structure in the nano GCN/GF sample grows uniformly across the GF surface, forming well-distributed nanostructures with strong adhesion. In contrast, the porous GCN/GF structure develops surface etching and hole formation due to gas release during synthesis, while the macro GCN/GF structure becomes over-aggregated, forming large lumps as a result of excessive urea precursor during the growth process.

The deconvoluted high-resolution XPS spectra of C 1s and N 1s (Fig. S3(a and b)) confirm the structural integrity of graphitic carbon nitride and its successful decoration in nano GCN/GF. The C 1s spectra (Fig. S3a) showed four characteristic components at 284.8, 286.3, 287.9, and 288.9 eV, corresponding respectively to graphitic carbon (C-C), C-N, C=N, and N-C=N linkages—the key bonding environments of the g-C_3N_4 framework [49]. For the Nano GCN/GF and Powder GCN samples, these carbon–nitrogen bonding states are clearly observed, whereas pristine GF displays only graphitic carbon without intrinsic C-N or C=N species. In the Nano GCN/GF sample, C=N is the dominant component (56.4 %), followed by N-C=N (18 %), C-N (13.5 %), and a minor C-C contribution (12.1 %), confirming the successful decoration on the GF surface. Powder GCN exhibits a similar trend, with C=N (56.8 %), C-C (20.8 %), N-C=N (12.9 %), and C-N (9.5 %), consistent with the polymeric g-C_3N_4 structure. In contrast, pristine GF shows predominantly C-C/C=C (55.8 %), along with adventitious or edge-type carbon (31.9 %) and a small C-O signal (12.3 %), indicating the absence of carbon–nitrogen functionalities prior to decoration. The enrichment of C-N and C=N species in the coated samples, therefore, provides strong evidence of effective g-C_3N_4 decoration.

The N 1s spectra (Fig. S3b) further support this conclusion. Both Nano GCN/GF and Powder GCN exhibit three typical nitrogen components: pyridinic N, pyrrolic N, and graphitic N. In Nano GCN/GF, pyridinic and pyrrolic nitrogen dominate (48.1 % and 46.8 %), with a small contribution from graphitic N (5.1 %), indicating a structure enriched in edge/defect-type nitrogen sites. Powder GCN contains relatively more pyridinic N (59.9 %) and less pyrrolic N (32.9 %), with a comparable graphitic N fraction (7.2 %), reflecting a more ordered heptazine/triazine framework [50]. As expected, pristine GF shows no nitrogen signal, confirming that all N-containing species originate from the g-C_3N_4 decoration. These observations collectively validate the successful decoration of g-C_3N_4 on the graphite felt and highlight structural differences between the Nano GCN/GF and Powder GCN materials. The nano GCN/GF electrode exhibits higher surface polarity (via C-N/C=N groups), improved wettability, and active nitrogen sites. These structural and chemical advantages significantly enhance electrolyte accessibility and charge-transfer kinetics, clearly indicating that the nano GCN/GF electrode is the optimized structure for further electrochemical evaluation.

3.1.6. BET specific surface area test

The specific surface area and pore size distribution of g-C_3N_4/GF were examined through nitrogen adsorption and desorption experiments. Brunauer-Emmett-Teller (BET) measurements utilize gas molecules to assess adsorption and desorption on the surface of the material, with nitrogen being the most common gas used in this process. Since g-C_3N_4 has a 2D layered structure with planar heptazine units stacking via π–π interactions, this limits nitrogen physisorption in the BET analysis. The relative pressure versus adsorption curves for different structures of graphite-phase carbon nitride (g-C_3N_4) decorated GF (GCN/GF) are shown in Fig. S4, and the data are summarized in Table 1. The BET specific surface area of the graphite felt is 6.89 m^2/g, while the porous GCN/GF surface area nearly doubles to 13.12 m^2/g. However, from the SEM and EDS results, it is evident that only a small amount of g-C_3N_4 grows on the surface of the graphite felt. This may be due to the formation of holes during heat treatment and reactions between carbon and nitrogen. The BET specific surface area of nano GCN/GF increased to 33.25 m^2/g, indicating an increase in surface area due to the layer stacking of g-C_3N_4, while macro GCN/GF had the largest specific surface area (34.62 m^2/g). These findings suggest that structured g-C_3N_4 decoration on GF (GCN/GF) promotes a more porous or better-dispersed nanostructure, exposing more surface sites and interlayer voids. However, the structure was polymerized due to excessive layer stacking, and this 2D π–π stacking structure of g-C_3N_4 showed an increase in surface area and porosity, which is beneficial for catalysis of vanadium ion redox reactions [51]. Nonetheless, macro-GCN/GF is more porous; it may exhibit slower electron transport or lower internal surface utilization due to uneven distribution of active sites or to less contact between g-C_3N_4 and the GF surface. Therefore, an optimized structure that balances high surface area, moderate pore size, and improved electrical contact with the conductive GF is vital for enhanced performance in VRFBs.

Table 1
BET measurement results of pristine GF and g-C_3N_4-decorated graphite felt (GCN/GF).

Sample	BET surface area (m^2/g)	Pore Volume (cm^3/g)	Pore size (Å)
Pristine GF	6.84	0.006	33.7
Porous GCN/GF	13.12	0.011	34.7
Nano GCN/GF	33.25	0.084	100.8
Macro GCN/GF	34.62	0.099	114.5

3.1.7. Electrochemical analysis

The electrochemical properties of the pristine GF electrode and the g-C_3N_4-decorated graphite felt (GCN/GF) electrode for the redox reaction of VO^{2+}/VO_2^+ were examined using the electroanalytical technique CV, performed at a scanning rate of 5 mV/s. The results are presented in Table 2. The measured CV curves are shown in Fig. 4a, and all samples display significant redox peaks, indicating that all electrodes exhibit a catalytic effect on the VO^{2+}/VO_2^+ couple. The electrocatalytic activity of different electrodes was investigated by comparing the oxidation peak current (I_{pa}) and reduction peak current (I_{pc}). Pristine GF has broader peaks and a lower current response, indicating slower kinetics and higher overpotential. In contrast, structured decorated GCN/GF electrodes demonstrate significantly higher peak current densities, indicating improved electrochemical activity and faster electron transfer. The higher capacitive background in structured decorated GCN/GF electrodes indicates a higher surface area, and the pronounced redox peaks confirm that faradaic (electron transfer) processes dominate the electrochemical behavior. Among all the samples, nano GCN/GF exhibited the smallest ΔE (270 mV), and this electrode showed the most significant peak current, indicating that the decoration of nanostructure g-C_3N_4 significantly enhances the electrochemical activity of GF. Its I_{pa} and I_{pc} are 52.57 mA/cm^2 and 51.84 mA/cm^2, respectively.

The peak currents of different samples are as follows: nano GCN/GF > porous GCN/GF > GF > macro GCN/GF. Microstructural surface analysis showed that during the synthesis process of porous GCN/GF, the surface of the graphite felt was significantly damaged, resulting in many irregularly etched holes. The electrochemical properties further confirmed this, which led to poor electron transfer characteristics. However, among all the samples, macro GCN/GF exhibited the lowest electrochemical activity due to pore blockage, hindrance in electron transport, or uneven distribution of active sites caused by the excessive accumulation of macrostructure g-C_3N_4 (macro GCN/GF) resulting from an overabundance of precursor during synthesis, as also observed in the SEM and EDS results. In agreement with the positive-side CV results, the negative-side CV of the nano-GCN/GF electrode also shows higher peak currents and reduced polarization compared to pristine GF, indicating enhanced reaction kinetics and improved reversibility on both electrodes (Fig. S5). The Randles–Sevcik plots for oxidation and reduction processes further confirmed the superior electrochemical performance of the nano-GCN/GF electrode, as illustrated in Fig. S6. All samples showed a linear relationship between peak current density and the square root of the scan rate, indicating diffusion-controlled redox processes [52]. The nano GCN/GF electrode exhibited the steepest slope, attributed to its large surface area, well-exposed active sites, and optimized morphology, all contributing to more efficient electron transfer and faster vanadium ion diffusion. Consequently, nano GCN/GF has the most balanced and pronounced peaks in both oxidation and reduction regions, reflecting better reversibility and the highest electrochemical activity for the VO^{2+}/VO_2^+ couple.

The electrochemical properties of graphite-phase carbon nitride (g-C_3N_4) decorated GF (GCN/GF) are further investigated using EIS through the Nyquist plot (Fig. 4b) and the Bode plot (Fig. 4c,d). The NOVA 2.1.8 software was utilized to fit the equivalent circuit model parameters. In this model, R_s denotes the ohmic impedance between the electrode and module, R_{ct} represents the charge transfer resistance at the electrode–electrolyte interface, and C signifies the double-layer capacitance from charge separation. The symbol Q represents a Constant Phase Element (CPE). CPEs are commonly used in EIS modeling to describe non-ideal capacitive behavior arising from surface roughness, porosity, or heterogeneous charge distribution at the electrode–electrolyte interface. The impedance of CPE is expressed as

$$Z_{CPE} = {}^{1}/_{Q_{Y_0}\,(j\omega)^{n}}$$

here Q_{Y_0} represent the magnitude, and exponent n (0–1) defines the deviation from ideal behavior. When ideal resister when n = 0, it behaves as an ideal capacitor for n = 0; when n = 0.5, it approximates a Warburg diffusion element [53]. EIS analysis results or fitted equivalent circuit model parameters of pristine GF and decorated graphite felt (GCN/GF) are given in Table 2. The impedance response was categorized by frequency: high frequency (HF: 10^4-10^2 Hz), mid frequency (MF: 10^2-1 Hz), and low frequency (LF: <1 Hz). HF generally relates to the solution resistance (R_s), representing the electrolyte resistance at the interface and the electrode material's electronic conductivity. However, no significant change is observed in this region, suggesting that g-C_3N_4 did not substantially enhance the electrode's electronic conductivity. Instead, the improved VRFB performance is primarily due to the structure of decorated GCN/GF, which increases porosity and the active sites. However, the MF and LF regions showed significant differences. They were associated with charge transfer processes (R_{ct}) and the Constant Phase Element Q with n = 0.90, respectively, where the Q element reflects the non-ideal capacitive behavior and surface heterogeneity of the decorated GCN/GF structure. As shown in Fig. 4b, nano GCN/GF exhibits the lowest charge transfer resistance (R_{ct}, 2.22 Ω), attributed to the compatibility of nano-structure g-C_3N_4 for stacking. During synthesis, it is effectively dispersed on the graphite surface felt without excessive polymerization, resulting in electrochemical activity and faster electron transfer. Table 2 shows the fitted exponent for the GCN/GF samples, particularly the Nano GCN/GF (n = 0.90), which significantly deviates from the n = 0.50 value required for ideal semi-infinite diffusion. Therefore, the element Q in the low-frequency region primarily reflects non-ideal capacitive behavior and surface heterogeneity (roughness, porosity) rather than pure mass transport limitation. The higher magnitude of Q observed for Nano GCN/GF directly reflects an increase in the electrochemically active surface area (or double-layer capacitance), which is consistent with more extensive ion infiltration into its highly porous structure. This extended surface area enhances electrode performance by activating more internal sites. This benefit is compounded by the lowest observed R_{ct} and the highest C value for the Nano GCN/GF, which collectively demonstrate a significant increase in ion-fiber contact and electrochemical activity, enabling better ion access and more efficient utilization of the electrode structure [54].

Porous GCN/GF decorated graphite felt fibers were damaged during the polymerization process, which hindered vanadium ion conduction, resulting in increased charge transfer impedance. In the Bode phase (Fig. 4c) plots, within the MF region, a single peak corresponding to the charge-transfer process is observed. For porous GCN/GF, the peak position shifts to a higher frequency, with the highest phase angle indicating more capacitive behavior. This suggests that charge transfer becomes a limiting process where charge is stored rather than transferred immediately [55]. From Fig. 4d, porous GCN/GF shows the

Table 2
EIS and CV analysis results of pristine GF and graphite-phase carbon nitride decorated graphite felt (GCN/GF).

	EIS					CV					
Samples	R_s (Ω)	R_{ct} (Ω)	C (*mF*)	Q_{y0}	Q_n	E_{pa} (V)	E_{pc} (V)	ΔE (mV)	I_{pc} (mA/cm^2)	I_{pa} (mA/cm^2)	I_{pc}/I_{pa}
GF	0.80	6.32	0.05	2.20	0.83	1.07	0.68	390	39.43	−48.05	0.82
Porous GCN/GF	0.80	12.11	0.01	0.59	0.66	1.12	0.62	520	43.72	−36.28	1.20
Nano GCN/GF	0.79	2.22	0.12	3.13	0.90	0.98	0.71	270	51.84	−52.57	0.95
Macro GCN/GF	0.79	6.64	0.08	2.66	0.90	1.15	0.65	500	34.64	−32.29	1.07

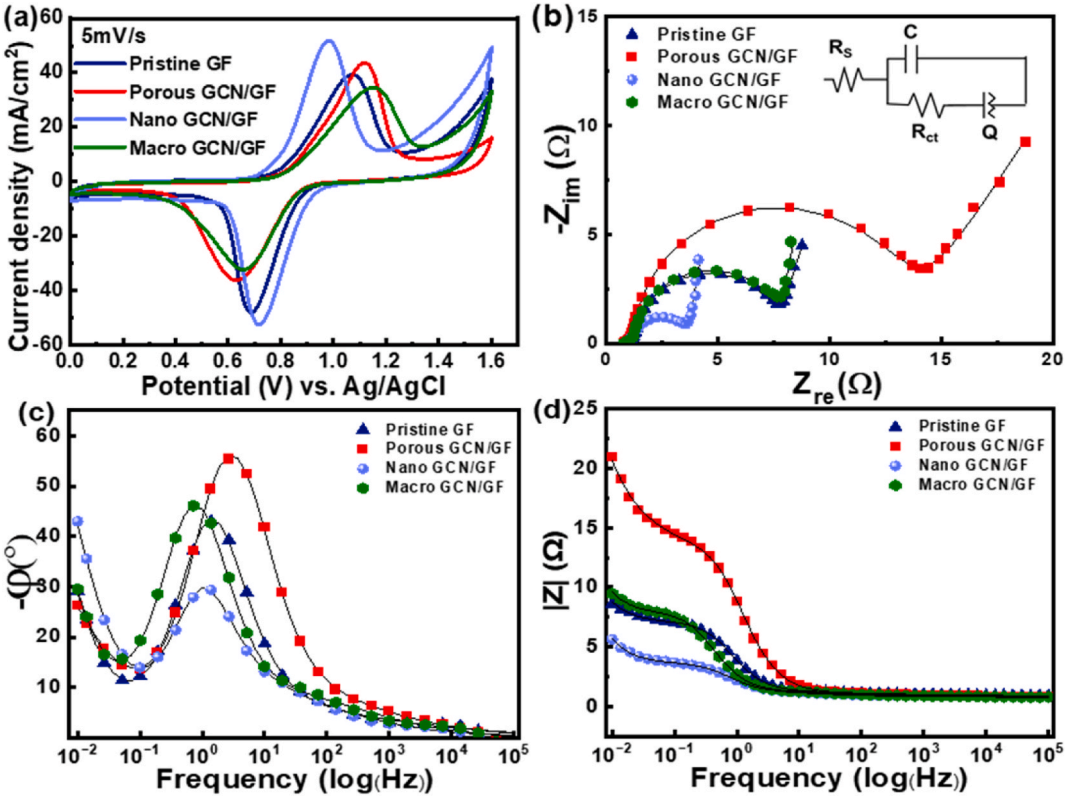

Fig. 4. Electrochemical properties of pristine graphite felt (GF), and various structures of graphite-phase carbon nitride decorated GF (GCN/GF) analysis by (a) cyclic voltammetry (CV) and electrochemical impedance spectroscopy (EIS) by (b) Nyquist Plot, (c), and (d) Bode Plot. (The black solid lines represent the fitting lines (NOVA 2.1.8 software), and the corresponding equivalent circuit diagram is shown as an inset in (b).

highest impedance at low frequency, indicating poor charge transfer at the electrode–electrolyte interface due to possible damage during the polymerization process. For nano-decorated GCN/GF, the highest phase angle at low frequency corresponds to mass transfer, while a peak at a relatively higher frequency corresponds to charge transfer, as shown in Fig. 4c. Its lowest phase angle indicates an improvement in interfacial charge transfer due to the optimized nano-structure GCN/GF, resulting from an increase in effective electrochemical surface area. It also exhibits the lowest impedance, indicating enhanced active sites and charge transfer in Fig. 4d. For macro-decorated GCN/GF, the peak shifts to a lower frequency, indicating slower ion dynamics and increased resistance caused by excess or agglomerated macrostructure g-C_3N_4, also observed in SEM and BET analysis. This blocks vanadium ion conduction and results in slower electron transport or reduced internal surface utilization, due to uneven active site distribution or limited contact between the g-C_3N_4 structure and the GF surface. Consequently, electrolyte access to active sites is restricted. As a result, the decrease in effective electrochemical surface area introduces mass-transfer resistance, alongside increased impedance due to the agglomeration of macro GCN/GF, as seen in Fig. 4d. Furthermore, the over-aggregation during the synthesis of macro GCN/GF caused a reduction in active sites, leading to poorer charge transfer than that of nano GCN/GF. This is attributed to the fact that decoration of the appropriate structure of g-C_3N_4 is essential to provide efficient reaction centers and reduce the charge transfer resistance during the VO^{2+}/VO_2^+ redox reaction. Therefore, nano-decorated GCN/GF demonstrates better electrochemical performance than the correlation analyzes mentioned earlier. Consequently, decorated nano GCN/GF was selected for the subsequent single-cell test.

3.1.8. Single battery test

Nano GCN/GF was used as the positive and negative electrodes to investigate its effect on the electrochemical performance of VRFB. Fig. 5a-d presents charge/discharge curves of nano GCN/GF compared to pristine at different current densities within a potential window of 0.6–1.6 V used for CV measurements. The overcharge potential of nano GCN/GF decreases with different current densities, resulting in a longer charging and discharging time of the single cell during the operation, as observed in the charging and discharging curves in Fig. 5. The charge/discharge times of the nano GCN/GF electrodes were 3965s, 1922s, 1145s, and 780s, at current densities 40 mA/cm^2, 60 mA/cm^2, 80 mA/cm^2, and 100 mA/cm^2, respectively.

The mean discharge voltage of the battery with nano-structured GCN/GF is always higher than that of the blank battery. The higher charge and discharge time for the nano GCN/GF electrode reconfirmed its enhanced charge storage capacity. This improvement results from decoration of nano GCN/GF's electrochemical properties, as EIS showed the lowest R_{ct}, indicating faster redox kinetics, while CV revealed a small peak separation (ΔE), demonstrating better reversibility. This decorated nano GCN/GF structure minimized agglomeration and maintained porosity, supporting ion transport and increasing active surface area. lower R_{ct} and C values indicate improved electrolyte infiltration and more effective use of the porous network, which helps sustain stable voltage during cycling. These enhancements explain the decorated nano GCN/GF superior performance and potential in high-efficiency VRFBs.

Fig. 6a shows the coulombic efficiency (CE), and the values of coulombic efficiencies of graphite felt and nano GCN/GF are similar, which means that the difference in utilization rate of graphite felt and decorated nano GCN/GF vanadium electrolyte is almost identical in the charging and discharging process. Fig. 6b shows the voltage efficiency of the nano GCN/GF; VE values are all higher than those of the GF because the nano GCN/GF is effectively decorated on the surface of the GF to increase the specific surface area and to improve and enhance the reaction rate of vanadium ions. Fig. 6c shows that the energy efficiency

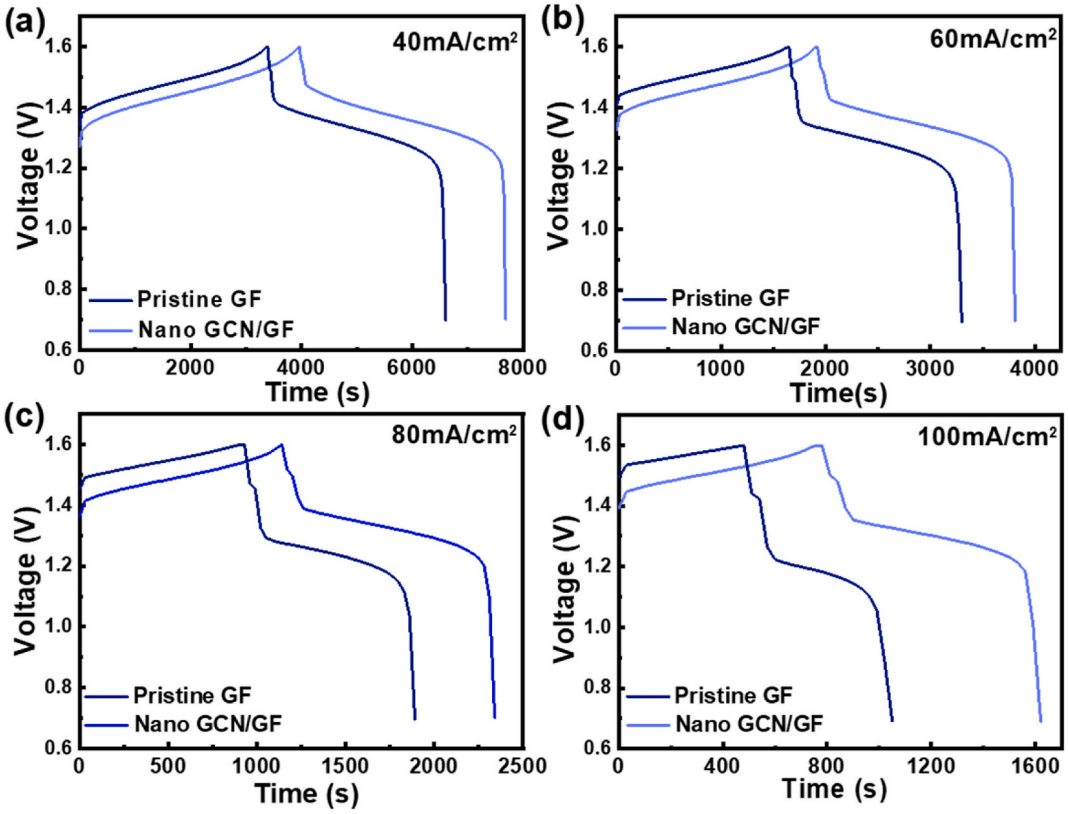

Fig. 5. Charge-discharge curve of nano GCN/GF in comparison with pristine GF at current densities of (a) 40, (b) 60, (c) 80, and (d) 100 mA/cm^2.

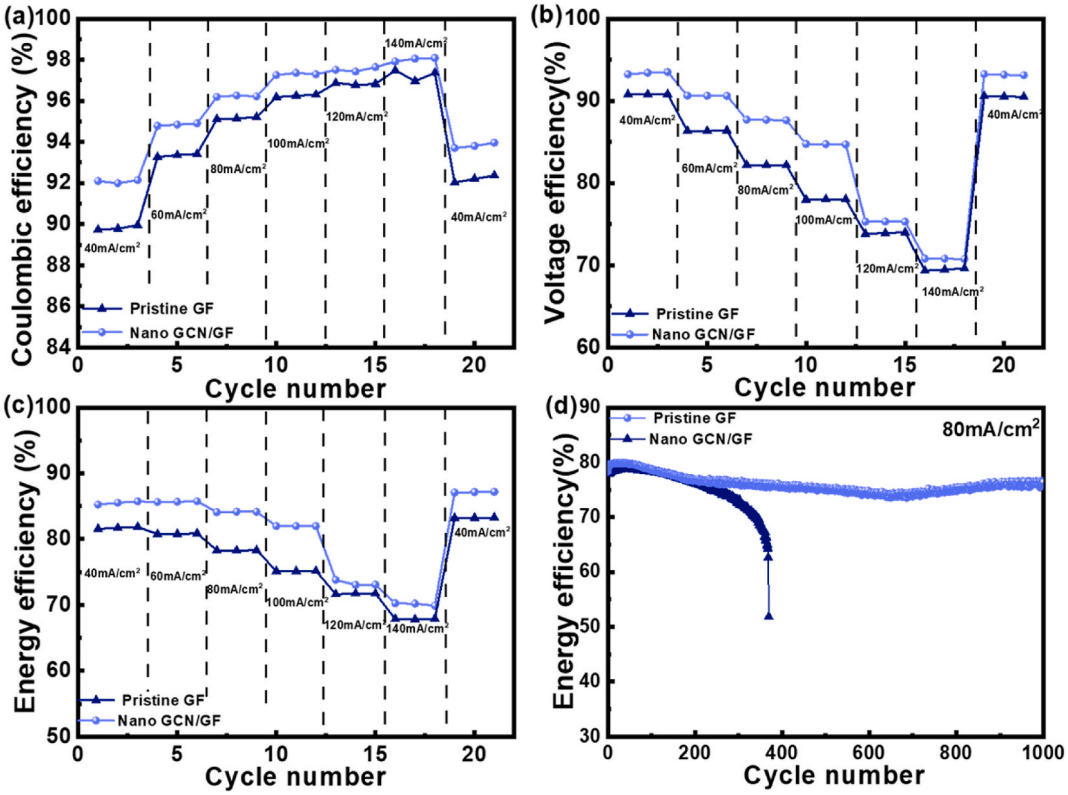

Fig. 6. Electrochemical performance of nano GCN/GF and pristine GF (a) CE, (b) VE, (c) EE, and (d) EE for pristine GF and nano GCN/GF at 80 mA/cm^2 for 1000 cycles.

(EE) of the graphite felt is only 78.05 %, and the energy efficiency of nano GCN/GF is 84.13 % at a current density of 80 mA/cm^2, which is an

increase of 6.08 %. The VE improves dramatically, and therefore, the EE also increases. This increase in VE indicates that the polarization degree of the battery decreases. Hence, decorated nano GCN/GF with many effective active centers as an electrode material significantly improves the battery's overall performance. Electrochemical performance of pristine GF and decorated nano GCN/GF at different current densities is listed in Table S2.

Long-term stability is a critical parameter for evaluating electrode performance in all-vanadium redox flow batteries. Fig. 6d presents the 1000-cycle charge–discharge tests of pristine GF and nano-GCN/GF electrodes at 80 mA cm^{-2}. The nano-GCN/GF electrode maintains an average energy efficiency above 75 % throughout the test, demonstrating excellent long-term durability. In contrast, the pristine GF exhibits rapid performance degradation and fails before 400 cycles. VRFB durability test during the 1000 cycles at the same current density by EE, CE, and VE is also shown in Fig. S7. These results confirm that the decorated nano-GCN/GF electrode provides significantly superior long-term cycling stability compared to pristine GF.

The improved cycling stability is due to π–π stacking, which enhances interfacial adhesion between the nano g-C_3N_4 structure and GF, reducing delamination and mechanical degradation during redox cycling. A larger surface area and increased wettability improve active sites and electrolyte penetration. Electrochemical data suggest low charge transfer resistance, indicating efficient transport even after extended operation. Taken together, these synergistic effects—originating from the material's intrinsic nanoscale morphology, chemical interaction, and electrochemical properties—enhance durability and energy efficiency, connecting decorated GCN/GF with nano-structure to long-term electrochemical reliability in VRFB systems.

4. Conclusion

In this study, to increase the surface area and hydrophilicity of graphite felt (GF), g-C_3N_4 is decorated on the GF surface. Different structures of g-C_3N_4 are created through a simple in-situ thermal polymerization process that involves impregnating the substrate (graphite felt) with varying urea precursor concentrations, followed by thermal treatment to directly decorate g-C_3N_4 structures on the GF. This process allows for uniform decoration of various graphite-phase carbon nitride (g-C_3N_4) structures on GF (GCN/GF) via precursor adsorption and in situ polymerization during controlled calcination. To optimize the decorated g-C_3N_4 structures for the best performance, multiple characterization techniques are used. Nano GCN/GF is identified as the optimal decorated structure, providing efficient reaction centers and lowering charge transfer resistance, which improves electrochemical performance. XRD results confirm the crystalline structure of all g-C_3N_4-decorated graphite felt (GCN/GF). SEM images show g-C_3N_4 decorating the surface of the graphite felt as different layered structures, and EDS indicates the presence of nitrogen atoms on the decorated nano GCN/GF surface. The hydrophilicity of the decorated GCN/GF is enhanced, as evidenced by contact angle tests, and BET analysis shows increased surface area and porosity. Nano-GCN/GF shows strong long-term durability, maintaining >75 % energy efficiency over 1000 cycles at 80 mA cm^{-2}, whereas pristine GF degrades quickly and fails even before 400 cycles. This confirms the clearly superior cycling stability of nano-GCN/GF. These findings suggest that decorating GF with an optimized g-C_3N_4 structure is a promising approach to enhance electrode electrochemical performance. The synergistic effects—arising from its intrinsic nanoscale morphology, chemical interactions, and electrochemical properties—improve durability and energy efficiency, thereby linking nanostructured GCN/GF to long-term electrochemical reliability in VRFB systems. Overall, this work may guide the development of high-efficiency electrodes for VRFB applications.

CRediT authorship contribution statement

Iqra Shaheen: Writing – original draft, Methodology, Investigation. **Wei-Hao Chiu:** Writing – review & editing, Data curation. **Yu-Xian Lee:** Investigation, Data curation. **Shih-Hsuan Chen:** Writing – review & editing, Formal analysis. **Jen-Fu Hsu:** Writing – review & editing. **Kun-Mu Lee:** Writing – review & editing, Supervision.

Declaration of competing interest

The authors declare that they have no known competing financial interests or personal relationships that could have appeared to influence the work reported in this paper.

Acknowledgments

The authors thank the support from National Science and Technology Council, Taiwan (Grant Number: 112-2221-E-182-020-MY2), Chang Gung University, Taoyuan, Taiwan (URRPD2R0011) and Chang Gung Memorial Hospital, Linkou, Taiwan (CMRPD2N0072).

Appendix A. Supplementary data

Supplementary data to this article can be found online at https://doi.org/10.1016/j.jpowsour.2025.239216.

Data availability

The data that has been used is confidential.

References

[1] R. López-Vizcaíno, E. Mena, M. Millán, M.A. Rodrigo, J. Lobato, Performance of a vanadium redox flow battery for the storage of electricity produced in photovoltaic solar panels, Renew. Energy 114 (2017) 1123–1133, https://doi.org/10.1016/j.renene.2017.07.118.

[2] D. Zha, Z.P. Bhat, K.-H. Lai, F. Yang, Z. Jiang, S. Zhong, X. Hu, Data-centric artificial intelligence: a survey, ACM Comput. Surv. 57 (2025) 1–42, https://doi.org/10.1145/3711118.

[3] R. Meirbekova, D. Bonciani, D.I. Olafsson, A. Korucan, P. Derin-Güre, V. Harcouët-Menou, W. Bero, Opportunities and challenges of geothermal energy: a comparative analysis of three European cases—Belgium, Iceland, and Italy, Energies 17 (2024) 4134, https://doi.org/10.3390/en17164134.

[4] A.Z. Weber, M.M. Mench, J.P. Meyers, P.N. Ross, J.T. Gostick, Q. Liu, Redox flow batteries: a review, J. Appl. Electrochem. 41 (2011) 1137–1164, https://doi.org/10.1007/s10800-011-0348-2.

[5] H. Fan, K. Liu, X. Zhang, Y. Di, P. Liu, J. Li, B. Hu, H. Li, M. Ravivarma, J. Song, Spatial structure regulation towards armor-clad five-membered pyrroline nitroxides catholyte for long-life aqueous organic redox flow batteries, eScience 4 (2024) 100202, https://doi.org/10.1016/j.esci.2023.100202.

[6] I. Shaheen, et al., MOF-& COF-integrated composite separators/membranes: innovations for sustainable and high-performance redox flow batteries, Sep. Purif. Technol. 343 (2025) 134157, https://doi.org/10.1016/j.seppur.2025.134157.

[7] D. Zhang, X. Zhang, C. Luan, B. Tang, Z. Zhang, N. Pu, K. Zhang, J. Liu, C. Yan, Zwitterionic interface engineering enables ultrathin composite membrane for high-rate vanadium flow battery, Energy Storage Mater. 49 (2022) 471–480, https://doi.org/10.1016/j.ensm.2022.04.033.

[8] D. Cheng, Y. Li, J. Zhang, M. Tian, B. Wang, Z. He, L. Dai, L. Wang, Recent advances in electrospun carbon fiber electrode for vanadium redox flow battery: properties, structures, and perspectives, Carbon 170 (2020) 527–542, https://doi.org/10.1016/j.carbon.2020.08.058.

[9] W. Wu, K. Wu, L. Han, P. Zheng, H. Fu, Z. Xu, Z. Hu, X. He, M. Ding, C. Jia, Advanced electrode decorated with peanut-shell-derived carbon for vanadium redox flow battery, J. Alloys Compd. 968 (2023) 171946, https://doi.org/10.1016/j.jallcom.2023.171946.

[10] Z. Hu, Z. Miao, Z. Xu, X. Zhu, F. Zhong, M. Ding, J. Wang, X. Xie, C. Jia, Carbon felt electrode modified by lotus seed shells for high-performance vanadium redox flow battery, Chem. Eng. J. 450 (2022) 138377, https://doi.org/10.1016/j.cej.2022.138377.

[11] Y. Huang, J. Xu, X. Huang, X. He, J. Cao, C. Jia, M. Ding, Advanced vanadium redox flow battery facilitated by synergistic effects of the Co_2P-Modified electrode, ACS Sustain. Chem. Eng. 12 (2024) 12837–12844, https://doi.org/10.1021/acssuschemeng.4c03551.

[12] X. He, L. Li, S. Yan, H. Fu, F. Zhong, J. Cao, M. Ding, Q. Sun, C. Jia, Advanced electrode enabled by lignin-derived carbon for high-performance vanadium redox

flow battery, J. Colloid Interface Sci. 653 (2024) 1455–1463, https://doi.org/10.1016/j.jcis.2023.10.005.
[13] H. Fu, X. Bao, M. He, J. Xu, Z. Miao, M. Ding, J. Liu, C. Jia, Defect-rich graphene skin modified carbon felt as a highly enhanced electrode for vanadium redox flow batteries, J. Power Sources 556 (2023) 232443, https://doi.org/10.1016/j.jpowsour.2022.232443.
[14] A. Kaur, K. Il Jeong, S. Su Kim, J. Woo Lim, Optimization of thermal treatment of carbon felt electrode based on the mechanical properties for high-efficiency vanadium redox flow batteries, Compos. Struct. 290 (2022) 115546, https://doi.org/10.1016/j.compstruct.2022.115546.
[15] M.K. Singh, M. Kapoor, A. Verma, Recent progress on carbon and metal based electrocatalysts for vanadium redox flow battery, WIREs Energy Environ 10 (2021) e393, https://doi.org/10.1002/wene.393.
[16] L. Wei, T. Zhao, L. Zeng, X. Zhou, Y. Zeng, Copper nanoparticle-deposited graphite felt electrodes for all vanadium redox flow batteries, Appl. Energy 180 (2016) 386–391, https://doi.org/10.1016/j.apenergy.2016.07.134.
[17] Y. Jiang, Z. Liu, Y. Ren, A. Tang, L. Dai, L. Wang, S. Liu, Y. Liu, Z. He, Maneuverable B-site cation in perovskite tuning anode reaction kinetics in vanadium redox flow batteries, J. Mater. Sci. Technol. 186 (2024) 199–206, https://doi.org/10.1016/j.jmst.2023.12.005.
[18] S. Zhang, L. Ma, Y. Wu, M. Xie, W. Liu, H. Jiang, B. Du, Y. Jiang, L. Wang, L. Dai, J. Zhu, Z. He, Constructing structural defects on perovskite surface to accelerate electrode kinetics for vanadium Redox flow batteries, Small 21 (2025) e06245, https://doi.org/10.1002/smll.202506245.
[19] Z. He, M. Li, Y. Li, C. Li, Z. Yi, J. Zhu, L. Dai, W. Meng, H. Zhou, L. Wang, ZrO_2 nanoparticle embedded carbon nanofibers by electrospinning technique as advanced negative electrode materials for vanadium redox flow battery, Electrochim. Acta 309 (2019) 166–176, https://doi.org/10.1016/j.electacta.2019.04.100.
[20] D.M. Kabtamu, J.-Y. Chen, Y.-C. Chang, C.-H. Wang, Electrocatalytic activity of Nb-doped hexagonal WO_3 nanowire-modified graphite felt as a positive electrode for vanadium redox flow batteries, Electrochim. Acta 220 (2016) 517–528, https://doi.org/10.1039/C6TA03936G.
[21] H. Zhou, J. Xi, Z. Li, Z. Zhang, L. Yu, L. Liu, X. Qiu, L. Chen, CeO_2 decorated graphite felt as a high-performance electrode for vanadium redox flow batteries, RSC Adv. 4 (2014) 61912–61918, https://doi.org/10.1039/c4ra12339e.
[22] X. Wu, H. Xu, L. Lu, H. Zhao, J. Fu, Y. Shen, P. Xu, Y. Dong, PbO_2-modified graphite felt as the positive electrode for an all-vanadium redox flow battery, J. Power Sources 250 (2014) 274–278, https://doi.org/10.1016/j.jpowsour.2013.11.021.
[23] D.M. Kabtamu, J.-W. Su, A.M. Demeku, Z.-J. Huang, G.-C. Chen, C.-H. Wang, High-performance graphite felt electrode loaded with oxygen-vacancy-rich $NiWO_4$ nanowires for vanadium redox flow batteries, J. Power Sources 628 (2025) 235929, https://doi.org/10.1016/j.jpowsour.2024.235929.
[24] J. Bao, W. Yang, K. Xu, Z. Li, Y. Kong, L. Sun, Y. Shi, Hierarchical carbon shell@C_3N_4 incorporated graphite felt as electrode for vanadium redox flow batteries, J. Power Sources, Journal of Power Sources 642 (2025) 236741, https://doi.org/10.1016/j.jpowsour.2025.236741.
[25] Q. Li, D. Pei, X. Zhang, H. Sun, Boosting performance of $Ti_3C_2T_X$/Bi modified graphite felt electrode for all-vanadium redox flow battery, Electrochim. Acta 473 (2024) 143439, https://doi.org/10.1016/j.electacta.2023.143439.
[26] J. Ji, C. Noh, M. Shin, S. Oh, Y. Chung, Y. Kwon, D.-H. Kim, Vanadium redox flow batteries using new mesoporous nitrogen-doped carbon coated graphite felt electrode, Appl. Surf. Sci. 611 (2023) 155665, https://doi.org/10.1016/j.apsusc.2022.155665.
[27] Z. Zhang, J. Xi, H. Zhou, X. Qiu, KOH etched graphite felt with improved wettability and activity for vanadium flow batteries, Electrochim. Acta 218 (2016) 15–23, https://doi.org/10.1016/j.electacta.2016.09.099.
[28] N. Yun, J.J. Park, O.O. Park, K.B. Lee, J.H. Yang, Electrocatalytic effect of NiO nanoparticles evenly distributed on a graphite felt electrode for vanadium redox flow batteries, Electrochim. Acta 278 (2018) 226–235, https://doi.org/10.1016/j.electacta.2018.05.039.
[29] S. Qiao, Q. Zhou, M. Ma, H.K. Liu, S.X. Dou, S. Chong, Advanced anode materials for rechargeable sodium-ion batteries, ACS Nano 17 (2023) 11220–11252, https://doi.org/10.1021/acsnano.3c02892.
[30] Y. Han, X. Zhou, R. Fang, C. Lu, K. Wang, Y. Gan, X. He, J. Zhang, H. Huang, W. Zhang, Supercritical carbon dioxide technology in synthesis, modification, and recycling of battery materials, Carbon Neutralization 2 (2023) 169–185, https://doi.org/10.1002/cnl2.49.
[31] Y. Tang, X. Wang, J. Chen, X. Wang, D. Wang, Z. Mao, PVP-Assisted synthesis of g–C_3N_4–derived N-doped graphene with tunable interplanar spacing as high-performance lithium/sodium ions battery anodes, Carbon 174 (2021) 98–109, https://doi.org/10.1016/j.carbon.2020.12.010.
[32] J. Wang, S. Wang, A critical review on graphitic carbon nitride (g-C_3N_4)-based materials: preparation, modification and environmental application, Coord. Chem. Rev. 453 (2022) 214338, https://doi.org/10.1016/j.ccr.2021.214338.
[33] M. Pourmadadi, E. Rahmani, M.M. Eshaghi, A. Shamsabadipour, S. Ghotekar, A. Rahdar, L.F.R. Ferreira, Graphitic carbon nitride (g-C_3N_4) synthesis methods, surface functionalization, and drug delivery applications: a review, J. Drug Deliv. Sci. Technol. 79 (2023) 104001, https://doi.org/10.1016/j.jddst.2022.104001.
[34] L. Biswal, S. Nayak, K. Parida, Recent progress on strategies for the preparation of 2D/2D MXene/gC_3N_4 nanocomposites for photocatalytic energy and environmental applications, Catal. Sci. Technol. 11 (2021) 1222–1248, https://doi.org/10.1039/D0CY02156C.
[35] Y. Tang, X. Wang, J. Chen, X. Wang, D. Wang, Z. Mao, Templated transformation of g-C_3N_4 nanosheets into nitrogen-doped hollow carbon sphere with tunable nitrogen-doping properties for application in Li-ions batteries, Carbon 168 (2020) 458–467, https://doi.org/10.1016/j.carbon.2020.07.022.
[36] L. Bai, H. Huang, S. Yu, D. Zhang, H. Huang, Y. Zhang, Role of transition metal oxides in g-C_3N_4-based heterojunctions for photocatalysis and supercapacitors, Journal of Energy Chemistry, J. Energy Chem. 64 (2022) 214–235, https://doi.org/10.1016/j.jechem.2021.04.057.
[37] E. Muchuweni, E.T. Mombeshora, B.S. Martincigh, V.O. Nyamori, Graphitic carbon nitride-based new-generation solar cells: critical challenges, recent breakthroughs and future prospects, Sol. Energy 239 (2022) 74–87, https://doi.org/10.1016/j.solener.2022.04.039.
[38] A. Hayat, M. Sohail, J. Ali Shah Syed, A.G. Al-Sehemi, M.H. Mohammed, A.A. Al-Ghamdi, T. Taha, H. Salem AlSalem, A.M. Alenad, M.A. Amin, Recent advancement of the current aspects of g-C_3N_4 for its photocatalytic applications in sustainable energy system, Chem. Rec. 22 (2022) e202100310, https://doi.org/10.1002/tcr.202100310.
[39] B. He, M. Feng, X. Chen, J. Sun, Multidimensional (0D-3D) functional nanocarbon: promising material to strengthen the photocatalytic activity of graphitic carbon nitride, Green Energy Environ. 6 (2021) 823–845, https://doi.org/10.1016/j.gee.2020.07.011.
[40] Y. Li, Z. Xia, Q. Yang, L. Wang, Y. Xing, Review on g-C_3N_4-based S-scheme heterojunction photocatalysts, J. Mater. Sci. Technol. 125 (2022) 128–144, https://doi.org/10.1016/j.jmst.2022.02.035.
[41] M.C. Daugherty, S. Gu, D.S. Aaron, R.E. Kelly, Y.A. Gandomi, C.-T. Hsieh, Graphene quantum dot-decorated carbon electrodes for energy storage in vanadium redox flow batteries, Nanoscale 12 (2020) 7834–7842, https://doi.org/10.1039/D0NR00188K.
[42] L. Zhang, Z.-G. Shao, X. Wang, H. Yu, S. Liu, B. Yi, The characterization of graphite felt electrode with surface modification for H_2/Br_2 fuel cell, J. Power Sources 242 (2013) 15–22, https://doi.org/10.1016/j.jpowsour.2013.05.049.
[43] Y.-S. Hsiao, J.-H. Huang, H.-Y. Lin, W.K. Pang, M.-T. Hung, T.-H. Cheng, S.-C. Hsu, H.C. Weng, Y.-C. Huang, Surface-modified graphite felt incorporating synergistic effects of TiO_2 decoration, nitrogen doping, and porous structure for high-performance vanadium redox flow batteries, Surf. Coat. Technol. 484 (2024) 130785, https://doi.org/10.1016/j.surfcoat.2024.130785.
[44] P. Zhang, Y. Wang, Y. Zhou, H. Zhang, X. Wei, W. Sun, S. Meng, L. Han, Preparation and photocatalytic properties of magnetic g-C_3N_4/TNTs nanocomposites, Mol. Catal. 465 (2019) 24–32, https://doi.org/10.1016/j.mcat.2018.12.023.
[45] T. Narkbuakaew, P. Sujaridworakun, Synthesis of Tri-S-Triazine based g-C_3N_4 photocatalyst for cationic rhodamine B degradation under visible light, Top. Catal. 63 (2020) 1086–1096, https://doi.org/10.1007/s11244-020-01375-z.
[46] T. Thamaraikannan, P. Karthikeyan, A.R. Sasieekhumar, A. Rathinavelu, M. Poovarasan, R. Saravanakumar, P. Srinivasan, R. Rajavel, Electrochemical analysis of g-C_3N_4-ferulic acid composite on the glassy carbon electrode surface and its electrocatalytic activity of dopamine oxidation and sensing, Appl. Phys. A 131 (2025) 624, https://doi.org/10.1007/s00339-025-08705-6.
[47] H. Tran Huu, T.N. Ngoc, N.S.M. Viswanath, M.T. Nguyen, T.H.T. Kim, V. Vo, M. Van Tran, H.N. Phi, A new insight into high-performance NiS_2@g-C_3N_4 anode for lithium-ion batteries – a DFT calculation and ex-situ XPS approach, J. Power Sources 653 (2025) 237719, https://doi.org/10.1016/j.jpowsour.2025.237719.
[48] S.K. Kuila, S.K. Guchhait, D. Mandal, P. Kumbhakar, A. Chandra, C.S. Tiwary, T. K. Kundu, Dimensionality effects of g-C_3N_4 from wettability to solar light assisted self-cleaning and electrocatalytic oxygen evolution reaction, Chemosphere 333 (2023) 138951, https://doi.org/10.1016/j.chemosphere.2023.138951.
[49] A. Bashir, A.H. Pandith, A. Qureashi, L.A. Malik, Fe_3S_4 nanoparticles wrapped in a g-C_3N_4 matrix: an outstanding visible active Fenton catalysis and electrochemical sensing platform for lead and uranyl ions, New J. Chem. 47 (2023) 1548–1562, https://doi.org/10.1039/D2NJ04933C.
[50] Y. Chen, X. Zheng, J. Cai, G. Zhao, B. Zhang, Z. Luo, G. Wang, H. Pan, W. Sun, Sulfur doping triggering enhanced Pt–N coordination in graphitic carbon nitride-supported Pt electrocatalysts toward efficient oxygen reduction reaction, ACS Catal. 12 (2022) 7406–7414, https://doi.org/10.1021/acscatal.2c00944.
[51] Q. Han, N. Chen, J. Zhang, L. Qu, Graphene/graphitic carbon nitride hybrids for catalysis, Mater. Horiz. 4 (2017) 832–850, https://doi.org/10.1039/C7MH00379J.
[52] J. González, E. Laborda, Á. Molina, Voltammetric kinetic Studies of Electrode reactions: guidelines for detailed understanding of their fundamentals, J. Chem. Educ. 100 (2023) 697–706, https://doi.org/10.1021/acs.jchemed.2c00944.
[53] A.C. Lazanas, M.I. Prodromidis, Electrochemical impedance spectroscopy— a tutorial, ACS Meas. Sci. Au 3 (2023) 162–193, https://doi.org/10.1021/acsmeasuresciau.2c00070.
[54] K. Ariyoshi, Z. Siroma, A. Mineshige, M. Takeno, T. Fukutsuka, T. Abe, S. Uchida, Electrochemical impedance spectroscopy part 1: fundamentals, Electrochemistry 90 (2022), https://doi.org/10.5796/electrochemistry.22-66071, 102007-102007.
[55] P. Leuaa, D. Priyadarshani, D. Choudhury, R. Maurya, M. Neergat, Resolving charge-transfer and mass-transfer processes of VO^{2+}/VO_2^+ redox species across the electrode/electrolyte interface using electrochemical impedance spectroscopy for vanadium redox flow battery, RSC Adv. 10 (2020) 30887–30895, https://doi.org/10.1039/D0RA05224H.